An atom probe tomography study of the chemistry of radiation-induced dislocation loops in Zircaloy-2 exposed to boiling water reactor operation

Journal of Nuclear Materials 550 (2021) 152923

Contents lists available at ScienceDirect

Journal of Nuclear Materials

journal homepage: www.elsevier.com/locate/jnucmat

An atom probe tomography study of the chemistry of radiation-induced dislocation loops in Zircaloy-2 exposed to boiling water reactor operation

J. Eriksson[a,*], G. Sundell[a,1], P. Tejland[b], H.-O. Andrén[a], M. Thuvander[a]

[a] Dept. of Physics, Chalmers University of Technology, SE-412 96 Gothenburg, Sweden
[b] Studsvik Nuclear AB, SE-611 82 Nyköping, Sweden

ARTICLE INFO

Article history:
Received 16 December 2020
Revised 4 February 2021
Accepted 5 March 2021
Available online 9 March 2021

Keywords:
Zirconium alloys
Radiation damage
Dislocation loops
Clustering
Boiling water reactor
Atom probe tomography

ABSTRACT

This study is complementary to previous atom probe tomography (APT) studies of irradiation effects in the zirconium alloy Zircaloy-2. Using APT in voltage pulse mode, a difference in morphology was observed between clusters of Fe and Ni and clusters of Fe and Cr in Zircaloy-2 exposed to a high fast neutron fluence in a commercial boiling water reactor. The Fe–Ni clusters were disc-shaped with a diameter of 5–15 nm, whereas the Fe–Cr clusters were spheroidal with a diameter of approximately 5 nm. Both types of clusters appeared to be located at irradiation-induced <a>-type dislocation loops aligned in layers normal to the <c>-direction. The concentration of Fe was higher in the Fe–Cr clusters than in the Fe–Ni clusters. The dilute Fe–Ni clusters, which seem to be segregation of Fe and Ni inside the loops, had formed on all three families of first-order prismatic planes with some deviation from perfect <c>-axis alignment. The Fe–Cr clusters might be very small precipitates with a nucleation associated with the loops.

1. Introduction

Zirconium alloys are used in nuclear reactors as cladding tubes for the nuclear fuel. In boiling water reactors (BWRs) the alloy Zircaloy-2 is commonly used. The neutron radiation during reactor operation induces radiation damage in the form of small dislocation loops in the hexagonal Zircaloy matrix, the smallest only a few nm in size [1]. The loops are commonly named according to the direction of their Burgers vector; <a>-loops have Burgers vector only in the <a>-directions, and <c>-component loops have Burgers vector with a component in the <c>-direction. In neutron-irradiated Zr and Zr alloys, the Burgers vector of <a>-loops has been observed to be 1/3<1 1 –2 0> [1,2] and the Burgers vector of <c>-component loops 1/6<2 0 –2 3> [1,3]. The <a>-loops are found on or close to the prismatic lattice planes, and they align in arrays forming layers that are parallel to the basal planes [1,2]. The <c>-component loops are found on the basal planes [1,3].

The dislocation loops can be either of interstitial or of vacancy type. In neutron-irradiated Zr and Zr alloys, both types of <a>-loops have been found to co-exist in various ratios depending on irradiation temperature and neutron fluence and with large grain-to-grain variations [1,2]. The <c>-component loops have been observed only as vacancy type loops and only after irradiation to high neutron fluence [1,3]. After exposure to a fast neutron fluence ($E >$ 1 MeV) of 8.7–14.7 $\times$ 10^{25} n m^{-2} in a BWR, the number density of <a>-loops has been observed to be in the order of 10^{22} m^{-3} and the number density of <c>-component loops in the order of 10^{21} m^{-3} [4].

The alloying elements Fe, Cr, and Ni have a very low solubility in the Zircaloy matrix [5–9], and they are initially mainly located in second phase particles (SPPs) of the types $Zr(Fe,Cr)_2$ and $Zr_2(Fe,Ni)$ [10]. During reactor operation the $Zr(Fe,Cr)_2$ SPPs undergo amorphisation, while the $Zr_2(Fe,Ni)$ SPPs remain crystalline [11]. The alloying elements are dissolved from the SPPs, with preferential dissolution of Fe [12–14]. The onset of change in Fe/Ni ratio in $Zr_2(Fe,Ni)$ SPPs has been observed to occur after exposure to a neutron fluence that is higher than that for the onset of change in Fe/Cr ratio in $Zr(Fe,Cr)_2$ SPPs but lower than that of the material studied in this work [13,14]. After exposure to the fluence of the

* Corresponding author.
E-mail address: ejoha@chalmers.se (J. Eriksson).
[1] Now at Vitroprobe Analytics AB, Danska vägen 83, SE-416 59 Gothenburg, Sweden

https://doi.org/10.1016/j.jnucmat.2021.152923

material studied in this work, there are SPPs of both types that are not fully dissolved [13].

Experimental observations of clusters of Fe, Cr, and Ni after irradiation have been reported in e.g. [4,15,16]. Using atom probe tomography (APT), Sundell et al. observed spheroidal clusters of Fe and Cr, but virtually without Ni, aligned along parallel planes of the Zircaloy matrix, therefore believed to be related to <a>-loops [15]. Large variations in cluster composition and cluster number density between different grains were noted. In a more recent study, using transmission electron microscopy (TEM), Harte et al. found that clusters of either Fe and Ni or Fe and Cr form at <a>-loop positions [4]. They also observed that Sn was preferentially located between the layers of clusters of Fe and Ni. Using both APT and TEM, Sawabe and Sonoda observed that clusters located close to grain boundaries or partially dissolved $Zr(Fe,Cr)_2$ SPPs contained Fe and Cr, whereas clusters further away in the matrix contained Fe but not Cr [16]. They also estimated the matrix concentration of Fe to vary from 0.03 to 0.12 at.%. It should be noted that Sundell et al. analysed the metal very close to the oxide [15], as is also done in the present study, whereas Harte et al. used electropolished TEM foils [4] (making it likely that they studied the metal relatively far away from the metal/oxide interface) and Sawabe and Sonoda studied the intermediate portion between the inner and outer surfaces of their material [16].

Segregation of Ni to both interstitial and vacancy <a>-loops has been modelled by Dai et al., and their results suggest that Ni atoms segregate along the edge of 10 nm diameter vacancy loops and 18 nm diameter interstitial loops [17]. At interstitial loops of 10 nm diameter, Ni atoms instead accumulate inside the loops. In another study by Dai et al., the segregation of Fe to 10 nm diameter vacancy and interstitial <a>-loops was modelled [18]. The results are similar to those for Ni; Fe segregates to the edge of vacancy loops and to the inside of interstitial loops. Modelling by March-Rico et al. predicts that Fe is more likely than Cr, Ni, and Sn to segregate to the stacking faults of <a>-loops [19].

Under conditions of reactor operation, Zr alloys undergo irradiation growth, which means that dimensional changes occur while the volume remains constant [20]. The matrix expands in the <a>-directions and contracts in the <c>-direction [20]. Both <a>-loops and <c>-component loops are believed to be involved in irradiation growth, and the formation of <c>-component loops has been observed to correlate with the onset of a rapid increase in growth rate, termed breakaway growth [20,21]. The mechanisms of formation of <c>-component loops and their relation to irradiation growth are not fully understood. Harte et al. have proposed that <c>-component loops form by alignment of <a>-loops and have reported an anticorrelation between positions of <c>-component loops and positions of <a>-loops [4]. In addition to irradiation growth, Zr alloys are degraded by corrosion and hydrogen pickup. The alloying elements affect all these three degrading processes [20,22,23]. It is thus of interest to study the relation between radiation-induced dislocation loops and alloying elements.

In previous APT observations of clusters of alloying elements aligned in layers at expected positions of <a>-loops [15,16], the cluster shape does not match what is predicted for Fe and Ni in the modelling in [17,18]. Only spheroidal clusters of Fe and Cr, with varying Fe/Cr ratio, have been observed, with the exception of a study of β-treated Zircaloy-2 irradiated at 358 °C in a high-flux reactor (conditions different from those of commercial BWRs), where segregation of Fe, Cr, and Sn to ring-shaped clusters that were not clearly aligned was observed [24]. In that study, Ni was observed only in a few clusters. The present study aims at in greater detail investigating the distribution of Ni, the morphology of the clusters, and their relation to the loops. To get as high spatial resolution as possible, voltage pulse mode was used. APT analysis of Zr alloys in voltage pulse mode is more challenging than in laser pulse mode [6,25–28], and our use of voltage pulsing makes the present study significantly different compared to other APT studies of Zr alloys that have used laser pulsing [15,16,24,26–34] (although early one-dimensional (1D) atom probe studies of Zr alloys have used voltage pulsing [5,6,25]). The higher spatial resolution of voltage pulsing usually results in improved cluster detection [35] and better crystallographic information [36]. Due to the higher stress on the specimen during voltage pulsing, the risk of specimen fracture is larger than in laser pulse mode, usually resulting in fewer and smaller datasets. The results in this paper are, to our knowledge, the first presented APT data from a Zr alloy run in voltage pulse mode.

2. Material

In this work, the material studied was the same as that investigated by Sundell et al. [15], i.e. Zircaloy-2 of the Westinghouse designated LK3^{TM} type exposed to nine annual cycles of reactor operation in a commercial BWR at Kernkraftwerk Leibstadt in Switzerland. The content of alloying elements and major impurities in the material is presented in Table 1. In addition to the elements listed in Table 1, impurity levels of C and Al are also usually present in Zircaloy-2 [29,30]. More or less identical material exposed to three to nine annual cycles in the same reactor has been studied in previous work [4,13–15,37–52]. The rod average burnup of the material studied in this work was 78.7 MWd/kgU, and the sample fast neutron fluence ($E > 1$ MeV) was high, 16.5×10^{25} n m^{-2}. Using the conversion factor for BWRs in [53], this neutron fluence corresponds to 26.5 dpa. The average hydrogen content of the studied rod has been measured to 664 ± 94 wt ppm (roughly corresponding to 6 at.%) [13].

3. Experimental

The specimen preparation procedure was the same as that described by Sundell et al. [15]. Atom probe specimens were prepared in the hot-lab of Studsvik Nuclear AB using the focused ion beam–scanning electron microscopy (FIB–SEM) lift-out technique [54]. The lift-out was made from the metal, about 0.5–3 μm from the metal/oxide interface. An instrument of type Imago LEAP 3000X HR with a detection efficiency of 0.37 was used for the APT measurements. Voltage pulsing with a 20% pulse fraction was used. The pulse frequency was 200 kHz, and the detection rate was 1.0%. The specimen was held at a temperature of 70 K, and the pressure in the analysis chamber was in the order of 10^{-9} Pa. Data evaluation was done using the Cameca software IVAS 3.6.14.

One advantage when analysing Zircaloy-2 in voltage mode is that the evaporation field is higher than in laser mode, resulting in a high fraction of Ni atoms evaporating as Ni^{2+} ions and only a very low fraction as Ni^{+} [55]. Since there are spectral overlaps between Ni^{+} and Sn^{2+} isotopes, Ni can reliably be detected only as Ni^{2+}. Although evaporation of Fe^{2+} and Cr^{2+} occurs at a lower field than that for evaporation of Ni^{2+} [55], the effect of higher field is similar for Fe and Cr, minimising overlaps between Fe^{+} and ZrO^{2+} and between Cr^{+} and ZrC^{2+}. The combination of the higher field and the improved spatial resolution makes the information obtained from APT in voltage mode complementary to the information already obtained from previous APT work using laser mode. Due to the higher risk of specimen fracture when running Zr alloys in voltage mode, data from only two specimens were obtained, yielding approximately 4.8 and 3.7 million ions. Crystallographic information was obtained in the run with 4.8 million ions. The results of that run are presented in this paper. The results of the other successful run confirm the main observations made, but no crystallographic orientation has been determined for the reconstruction of that specimen.

Table 1
Content of alloying elements and major impurities in the material studied.

	Sn (%)	Fe (%)	Cr (%)	Ni (%)	O (%)	Si (ppm)	N (ppm)
wt%/wt ppm	1.32	0.17	0.10	0.05	0.13	70	50
at.%/at. ppm	1.01	0.28	0.17	0.08	0.74	230	320

The ratio of Zr^{3+} to Zr^{2+} was 0.8, giving an estimated field a little below 30 V/nm [55], justifying our use of the default value of 28 V/nm for Zr in the reconstruction in IVAS. At this high field, Cr, Fe, and Ni should evaporate essentially as divalent ions, and there should not be any Al^{+} or Si^{+} causing overlaps at 27 and 28 Da, respectively [55]. As the overlaps between Cr^{+} and ZrC^{2+}, between Fe^{+} and ZrO^{2+}, and between Ni^{+} and Sn^{2+} should affect only a small fraction of the Cr, Fe, and Ni ions, only divalent ions of these elements were used in the ranging. Since there are overlaps between two Ni^{2+} isotopes and Zr^{3+}, between the main Ni isotope and a minor Fe isotope, and between minor Fe and Cr isotopes, only the main peaks for Cr^{2+}, Fe^{2+}, and Ni^{2+} at 26, 28, and 29 Da, respectively, were used for quantification. The number of ions at these peaks were multiplied according to the natural isotopic abundance of the respective element, and the overlap between Fe and Ni at 29 Da was corrected for. The 28 Da peak, which in Fe-containing Zr alloys often can be ascribed to both CO^{+} and Fe^{2+} (at least when laser pulsing is used) [29], showed no sign of being a double-peak and was divided into minor parts to see if the left parts of it (corresponding to Fe^{2+}) were preferentially detected in the clusters and the right parts of it (possibly corresponding to CO^{+}) preferentially detected in the matrix. As no such preferential detection was observed, the peak was in its entirety ranged as Fe^{2+}.

4. Results

4.1. Mass spectrum

The mass spectrum with labelled peaks is shown in Fig. 1. From this it can be seen that a large amount of H was detected in the analysis. This is not surprising since the lift-out was made close to the metal/oxide interface, a region expected to have a higher H content than the rod average of 6 at.%. The measured H concentration (using peak decomposition) was 51 at.%, out of which only a minor part is expected to originate from adsorbed residual H_2 gas from the vacuum system. This is within the range of 20–60 at.% reported by Sundell et al. [15], using laser pulsing. In the mass spectrum, ZrH^{2+} was the only hydride species that appeared in substantial amounts. The possibility of hydride ion formation affecting the quantification of Cr, Fe, and Ni was investigated by comparing the peaks at 26.5, 28.5, and 29.5 Da with the peaks at 26, 28, and 29 Da, respectively. From this it was concluded that the impact of CrH^{2+}, FeH^{2+}, and NiH^{2+} on the results was negligible. No enrichment of H at any specific features in the reconstruction was observed. The high H concentration indicates that the specimen was a hydride phase at the time the measurement was made. Of the four hydride phases that have been observed in Zr and Zr alloys, our measured concentration of close to 50 at.% corresponds to the γ-phase, which has stoichiometry ZrH [56]. As H redistributes during cool-down and the amount of hydrides increases as the solubility decreases [56], the observed H distribution was likely not the same as that during reactor operation. Redistribution of H can also occur during sample preparation, e.g. in the FIB [57,58]. As the change in atomic positions of Zr is small between α-Zr and hydride phases (although the hydride phases have different crystallographic structures) [59,60], the microstructural features observed in our analysis can be assumed to be representative of the metal during reactor operation. Hence, H was not further considered.

The O concentration was 0.95 at.% (H excluded). As the analysis was from a region close to the metal/oxide interface, it is not surprising that the O concentration is slightly higher than the nominal content of the material (0.74 at.%). In Zircaloy corroded in autoclave, there is often an O diffusion profile into the metal (beneath the ZrO_2 oxide or a ZrO suboxide) starting with saturated metal with an O concentration of about 30 at.%, decreasing asymptotically over a distance up to a few 100 nm until the concentration of the metal matrix is reached [31,61].

Gallium, from the FIB preparation, was mainly located in a small region on one side of the specimen. In this region, the concentration was 2.5 at.% (H excluded), and outside of this region it was below 0.1 at.%. Therefore, the Ga damage is expected to be insignificant. For quantification, H, C, and Ga were excluded from the ranging, and ZrH and ZrC were ranged as Zr.

4.2. Reconstruction and crystallography

Crystallographic poles were observed in the ion density map. Fig. 2 shows the detector hit map with a superimposed stereographic projection and part of a pole figure for α-Zr ($c/a = 1.593$), enabling identification of the poles. At the two major poles observed, (0001) and (1 0 −1 3), the atomic planes of the matrix were visible. The poles were identified using the symmetry, knowledge of the approximate field-of-view (60°), and the main pole being (0001). An iterative process in which the field factor (k) and the image compression factor (ICF) were varied to get the correct plane spacing and the correct angle between the planes at the poles was undertaken to obtain an appropriate reconstruction. This yielded $k = 4.2$ and $ICF = 1.35$ (with an evaporation field of 28 V/nm). Finally, the analysed volume was rotated to get the sides of the IVAS cube oriented parallel with the <c>-axis and one of the <a>-axes of the matrix. Spatial distribution maps (SDMs) showing the plane spacing of the final reconstruction are included in Fig. 2.

4.3. Clusters and loops

When the whole reconstructed volume is viewed in a direction perpendicular to the <c>-direction (Fig. 3) the clusters align in layers that are parallel to the basal planes of the matrix, in the same way as observed previously by APT and TEM [4,15,16]. The height of each layer of clusters is 10–15 nm, and the layers are separated by a distance that varies a little but typically is around 5 nm. Three layers and parts of a fourth layer of clusters were detected before the specimen fractured. From Fig. 4, which shows a 1D profile along the <c>-direction of the whole reconstructed volume as shown in Fig. 3, it can be seen that Fe, Cr, and Ni are concentrated in the layers of clusters and that Sn is not concentrated in these layers.

In the analysis, two distinctly different types of clusters were identified based on visual assessment, one mainly consisting of Fe and Ni and one mainly consisting of Fe and Cr. About five times more Fe–Ni clusters than Fe–Cr clusters were found. Both types of clusters were present in all of the observed layers, and there was also a small number of clusters consisting of Fe, Ni, and Cr, some

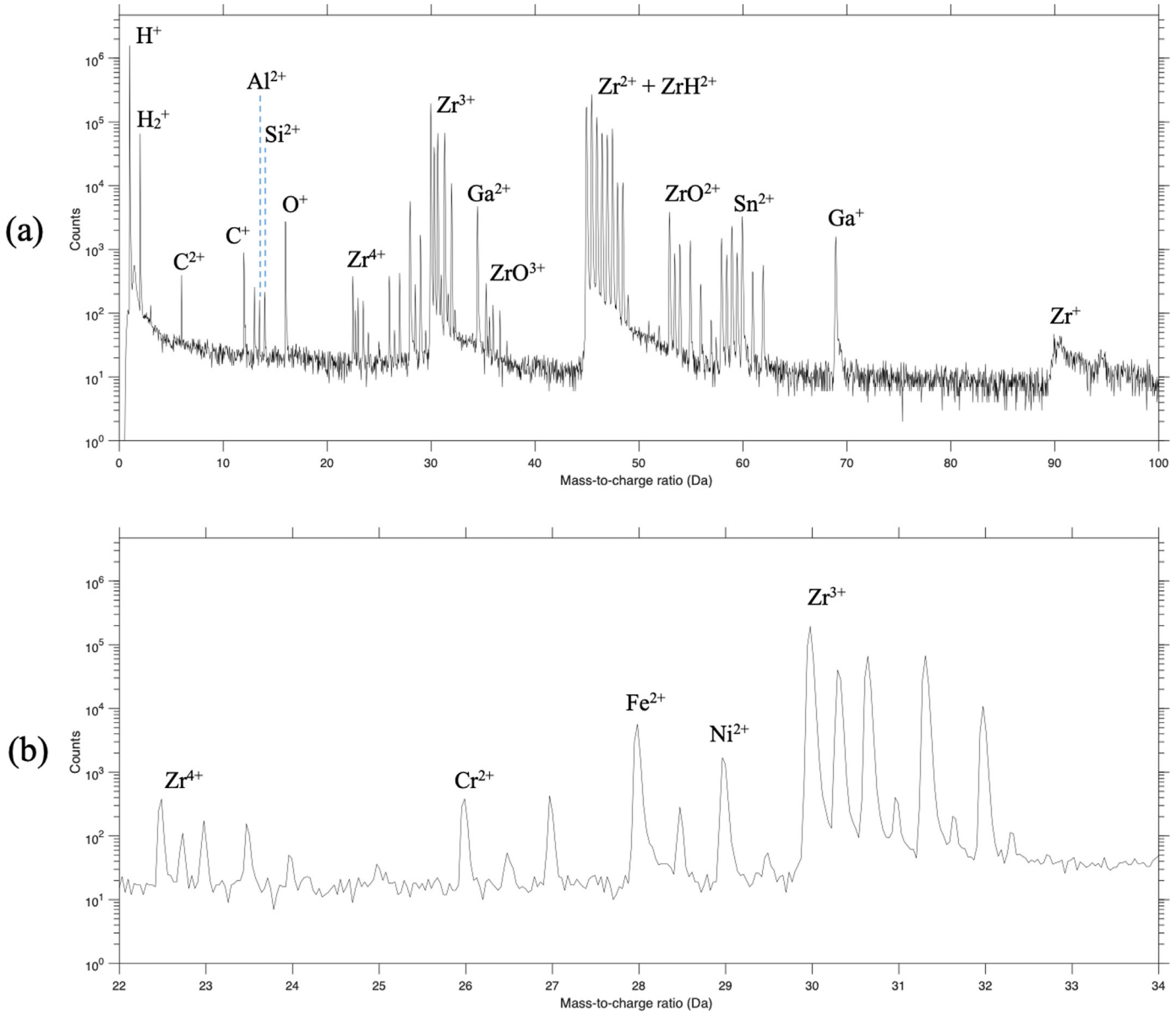

Fig. 1. Mass spectrum with most of the important peaks labelled. (a) Major part of the spectrum. (b) The part of the spectrum used for quantification of Cr, Fe, and Ni.

of which looked like if an Fe–Ni cluster and an Fe–Cr cluster had merged to form one joint cluster. The shape of the Fe–Ni clusters and the Fe–Cr clusters differed in that the former were disc-shaped and the latter spheroidal. (As there were no ionic density variations coinciding with any of the cluster types, this result seems not to be influenced by local magnification effects.)

Fig. 5 shows a comparison between the shape and size of a typical Fe–Ni cluster and a typical Fe–Cr cluster. The disc-shaped Fe–Ni clusters had a diameter of 5–15 nm and a thickness around 3 nm. The spheroidal Fe–Cr clusters had a diameter of approximately 5 nm. The <c>-direction of the matrix is indicated by the arrows in the figure. It was noted, both from the clusters shown in Fig. 5 and from the other clusters studied, that there was a small amount of Ni atoms in the Fe–Cr clusters and a very small amount of Cr atoms in the Fe–Ni clusters. The Cr atoms observed in the Fe–Ni clusters were usually located close to the outer parts of the clusters, whereas the Fe and Ni atoms were found both at the outer and the central parts of the clusters. There seemed to be no preferential segregation of any of the elements Fe, Cr, or Ni to the centre or to the edge of the Fe–Cr clusters. The total concentration in at.% of segregated Fe, Cr, and Ni was much higher in the Fe–Cr clusters than in the Fe–Ni clusters. The difference in composition between Fe–Ni clusters and Fe–Cr clusters is illustrated in Fig. 6 using proxigrams [62]. These proxigrams show that small amounts of Ni are present in the Fe–Cr clusters and that almost no Cr is present in the Fe–Ni clusters.

Table 2 shows the typical shape, size, area number density, composition, and number of atoms per cluster for the two main cluster types along with the composition of the matrix and the whole analysed volume. A total of 17 Fe–Ni clusters and four Fe–Cr clusters were used for calculation of compositions. For each of these clusters the composition was calculated as the ratio of the detected ions of the respective species to all detected ions in a region of interest (ROI) positioned well inside the cluster. The concentration of Fe in at.% was much higher in the dense Fe–Cr clusters than in the dilute Fe–Ni clusters. Using the average values for the evaluated clusters there were 5.3 times more Fe, Cr, and Ni atoms/nm^3 in the Fe–Cr clusters. The number of Fe, Cr, and Ni

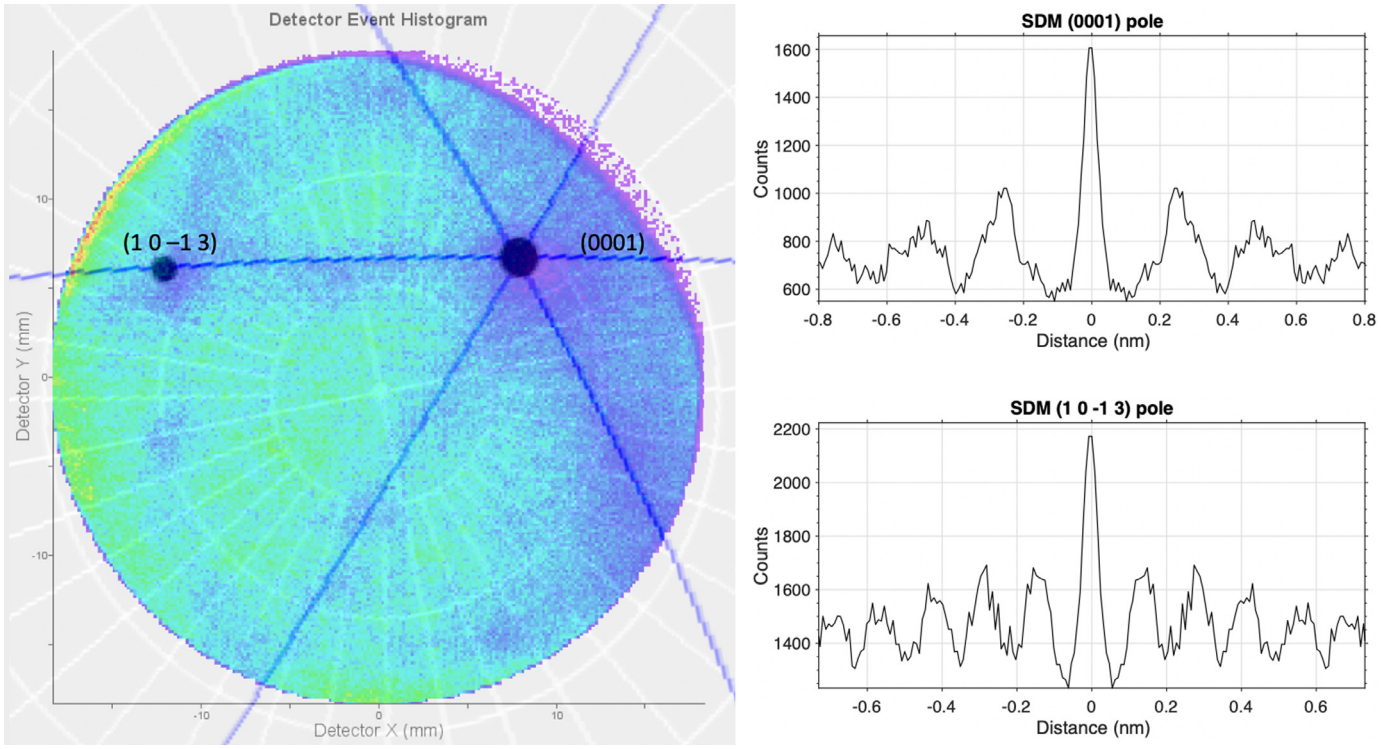

Fig. 2. Stereographic projection and part of a pole figure for α-Zr superimposed on the detector hit map with SDMs showing the interplanar spacing at the two major poles observed, (0001) and (1 0 –1 3).

Table 2
Shape, size, area number density, composition, and number of atoms per cluster for the two main cluster types along with the composition of the matrix and the whole analysed volume. The compositional balance is O, Al, and Si. The ± indicates one sample standard deviation.

Analysed region	Typical cluster shape	Typical cluster size	#clusters/cluster layer area (m^{-2})	at.%Fe	at.%Cr	at.%Ni	at.%Sn	at.%Zr	**#Fe+Cr+Ni atoms/cluster**
Fe–Ni clusters	Disc	$Ø$ = 5–15 nm t = 2–4 nm	5×10^{15}	5.8 ± 1.3	0.20 ± 0.24	3.0 ± 0.75	1.2 ± 0.54	89 ± 2.4	590 ± 281 (179–1171)
Fe–Cr clusters	Spheroid	$Ø$ = 5 nm	1×10^{15}	17 ± 1.9	10 ± 4.3	2.7 ± 1.9	0.93 ± 0.71	68 ± 1.3	490 ± 172 (234–604)
Matrix	-	-	-	0.044	0.0054	0.020	0.95	98	-
Whole volume	-	-	-	0.45	0.041	0.19	0.99	97	-

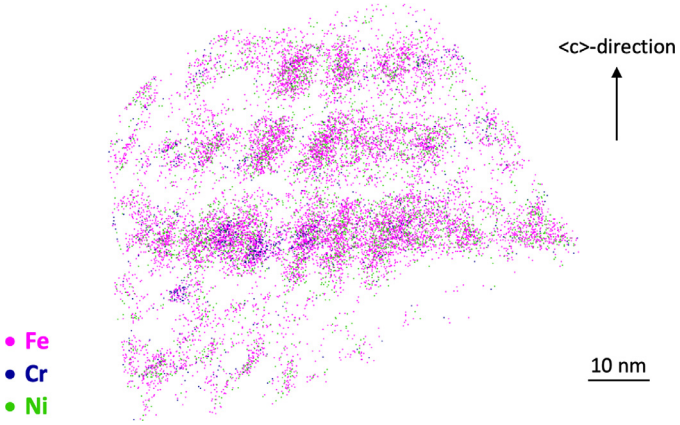

Fig. 3. The whole reconstructed volume viewed in a direction perpendicular to the <c>-direction.

atoms in each cluster was determined for 14 Fe–Ni clusters and four Fe–Cr clusters using ROIs containing all atoms of each cluster. Sn was on average not significantly enriched in the clusters, and the Sn concentration varied largely between the individual clusters. The matrix composition was estimated from what was on the lower gradient side of isoconcentration surfaces of 1 at.% Fe+Cr+Ni (voxel size 1 nm^3 and delocalisation 3 × 3 × 1.5 nm^3).

Cylindrical ROIs across the central parts of five Fe–Ni discs, with the discs oriented perpendicular to the cylinder axis, and four Fe–Cr clusters were used to measure the number of atoms in the part of the cluster covered by the ROI. Hence, the ROI diameter was smaller and the ROI length longer than the extent of each cluster. Assuming segregation to one plane, the number of Fe, Cr, and Ni atoms thus obtained divided by the area of the circular face of the cylinder (taking the detection efficiency into account) gives the number of segregating atoms of these species associated to that plane. This number was 9.2 ± 1.8 atoms/nm^2 for the Fe–Ni clusters and 38 ± 14 atoms/nm^2 for the Fe–Cr clusters. The corresponding number of monolayers (MLs) of an Fe face-centred cubic (FCC) (111) atomic plane is 0.52 for the Fe–Ni clusters and 2.2 for the Fe–Cr clusters. These values suggest that Fe–Ni clusters might be described as a segregation to one plane associated with a dislocation loop (as the value is clearly smaller than one), but probably not Fe–Cr clusters (as the value is clearly larger than one).

The Fe–Ni clusters were oriented in directions approximately 60° apart from each other, roughly matching the six sides of a hexagon, parallel with the <a>-directions. This is what is to be ex-

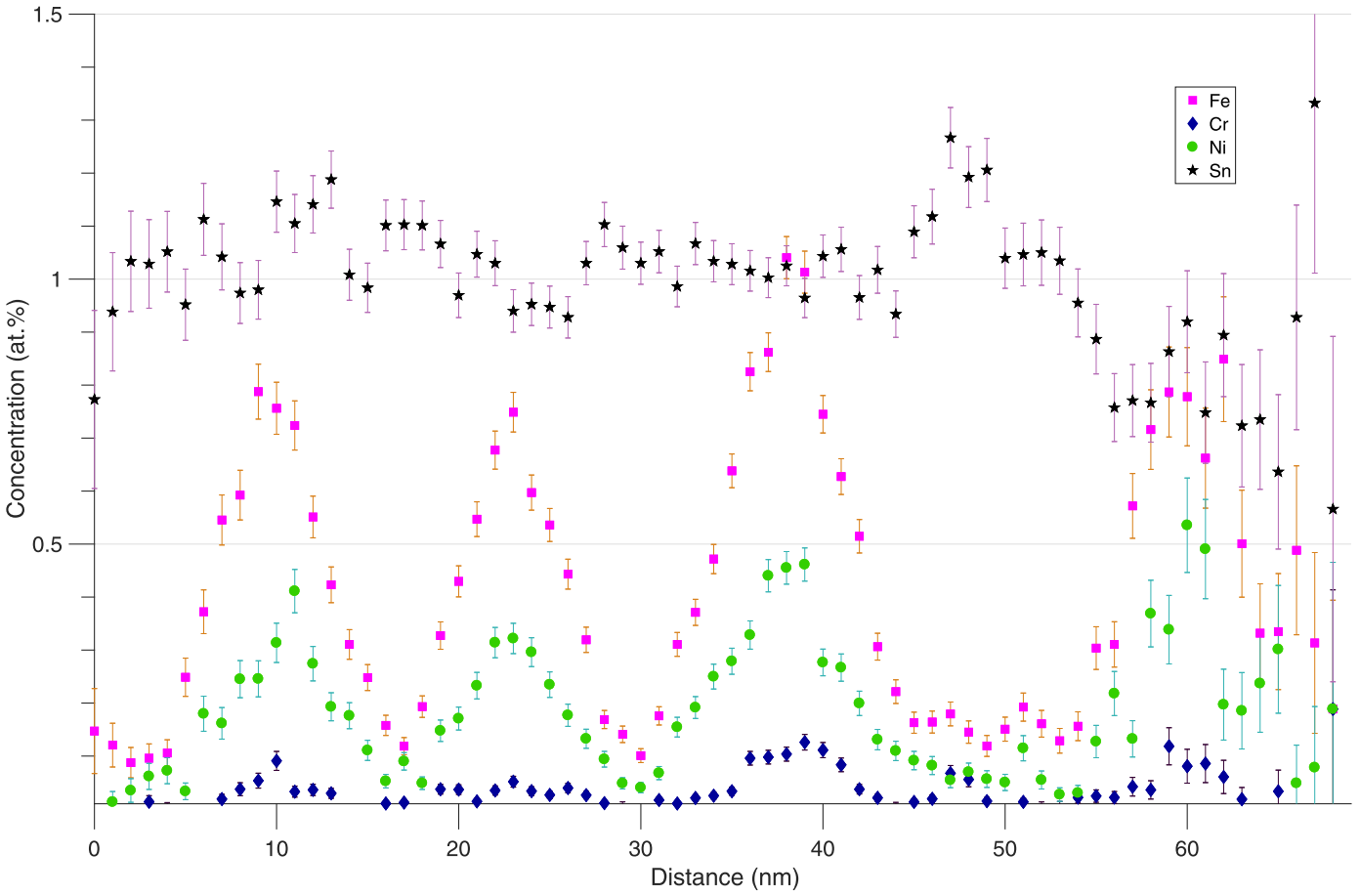

Fig. 4. 1D profile along the <c>-direction of the whole reconstructed volume. The profile runs from top (corresponding to 0 nm at the abscissa) to bottom in relation to Fig. 3. Values equal to zero (mainly Cr) are not displayed. The error bars (smaller than the data markers where not visible) represent one standard deviation of the counting statistics.

pected for <a>-loops. It can be noted that when a thin slice of one layer of clusters is viewed in the perspective in Fig. 7 the discs are located at planes that are close to the first-order prismatic planes (i.e. the {1 0 −1 0} planes) and that all three families of first-order prismatic planes are present in the same layer of clusters, seemingly without forming any ordered structure. As there is an angle between the cluster discs and the <c>-axis (Fig. 3 and Fig. 5), it is evident that the Fe–Ni clusters were not found on the prismatic planes of the hexagonal structure, but on planes that were inclined compared to the prismatic planes. The tilt angle (the complementary angle to the angle between the disc plane normal and the <c>-direction) was measured for 16 clusters, giving a range of 7°–36°, with an average angle of 22°. Experimental observations of <a>-loop dislocations being slightly inclined to the prismatic planes have been made in previous TEM studies [2,63,64], and <a>-loops having preferred habit planes that are close to, but not exactly, prismatic have been predicted in modelling [65]. No observation of <c>-component loops was made.

5. Discussion

From the results it is clear that the studied region was rich in Ni and Fe. Previous studies indicate that regions rich in Cr and Fe, containing a high density of Fe–Cr clusters, are more common [15,16]. Our observations should thus not be interpreted as general for the whole volume of irradiated metal, but be regarded as what it looks like in parts of the metal where the Ni content is high, at least close to the metal/oxide interface (the region studied here). A discussion of our results in the context of previous studies follows below.

A significant dissolution of both types of SPPs has been observed in the studied material after exposure to the high neutron fluence, although there were SPPs of both types that were not completely dissolved [13]. Originally, the material had a grain size of 4 μm, a mean SPP size (diameter) of 84 nm, and a mean distance between SPPs of 0.3 μm [66] so that each grain had contact with many SPPs. However, due to the dissolution of SPPs, and also to the smaller grain size resulting from formation of subgrains, which is known to occur close to the metal/oxide interface (the region studied here) because of oxidation-induced creep deformation [67], some grains may after exposure have no direct contact with an SPP, or at least not with both types of SPPs. According to Valizadeh et al., the SPP number density has decreased from 6.4×10^{19} m^{-3} in unirradiated reference material to 1.0×10^{19} m^{-3} (corresponding to a mean distance between SPPs of 0.46 μm) after nine cycles of reactor operation in the material studied here but at a position exposed to a slightly higher fluence of 17.9×10^{25} n m^{-2} [13]. However, the previous APT study by Sundell et al. showed many Fe–Cr clusters but virtually no Fe–Ni clusters [15]. Also in the study by Sawabe and Sonoda, clusters containing Ni were not observed [16]. Cockeram et al. observed a few Ni-containing clusters in one out of a total of five Zircaloy-2 specimens, albeit after exposure at higher temperature and flux than BWR conditions [24]. In the study by Sundell et al., a striking difference between different grains, with large differences in local chemistry, including cluster chemistry, was found [15]. This indicates that each grain has a

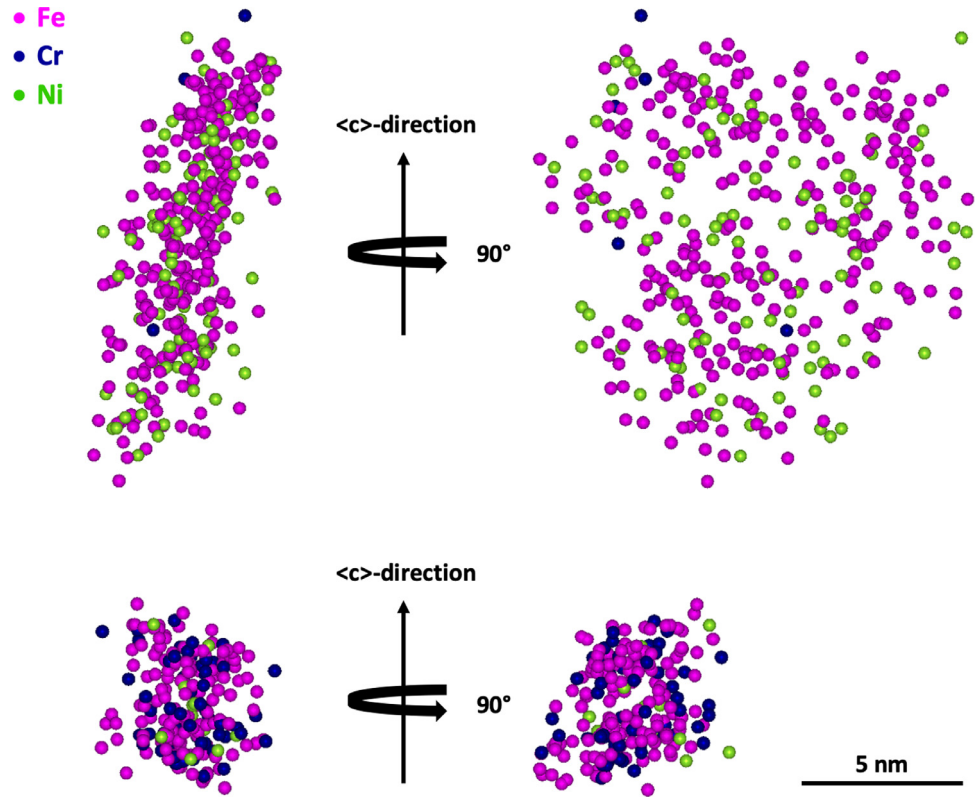

Fig. 5. (a) A typical Fe–Ni cluster viewed in two directions perpendicular to each other. (b) A typical Fe–Cr cluster viewed in two directions perpendicular to each other. The Fe–Ni cluster is disc-shaped, and the Fe–Cr cluster is spheroidal. The <c>-direction of the hexagonal matrix is indicated by the arrows.

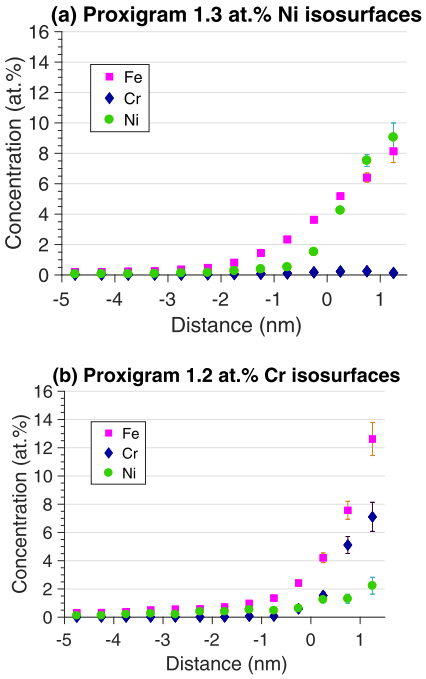

Fig. 6. (a) Proxigram for Ni isosurfaces of 1.3 at.%. (b) Proxigram for Cr isosurfaces of 1.2 at.%. (Voxel size was 1 nm^3 and delocalisation 3 × 3 × 1.5 nm^3 in both (a) and (b).) The error bars (smaller than the data markers where not visible) represent one standard deviation of the counting statistics.

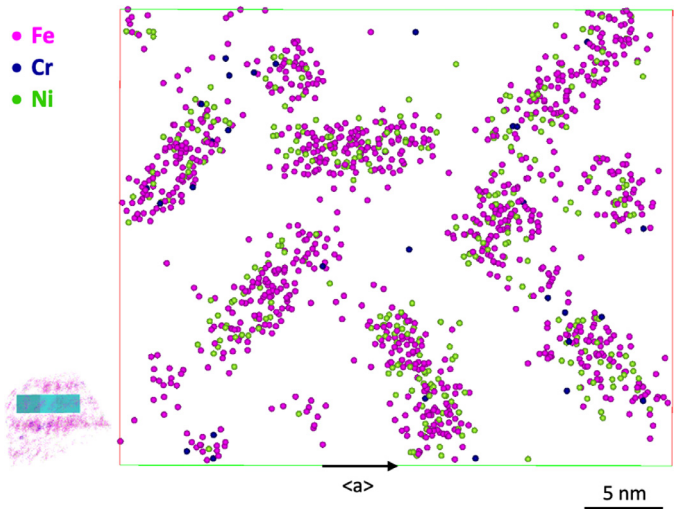

Fig. 7. A 6 nm slice of a region containing only Fe–Ni clusters. The blue ROI in the insert indicates this region, which in the main figure is viewed from below. Thus, the slice through the cluster discs is viewed in the <c>-direction. The green axis of the box is in one of the <a>-directions. (For interpretation of the references to colour in this figure legend, the reader is referred to the web version of this article.)

separate chemistry, probably determined by its contact with dissolving SPPs. From the study by Sawabe and Sonoda it seems that Fe–Cr clusters are mainly located close to dissolving Fe–Cr SPPs and close to grain boundaries [16], suggesting the distance to SPPs being one factor influencing local chemistry. The local chemistry is probably also affected by anisotropic diffusion of Fe, Cr, and Ni, faster matrix diffusion of Fe and Ni compared to Cr, and faster diffusion at grain boundaries than in the matrix [68]. Due to the fast grain boundary diffusion, the subgrains could effectively be isolated from each other. One possible explanation for the difference between the present results and those of Sundell et al. [15] could

be that the dissolving or dissolved SPP closest to the analysed grain differed in type between the two sets of analyses, i.e. Fe–Ni SPPs were closer to the specimen volumes studied here and Fe–Cr SPPs were closer to the specimen volumes studied by Sundell et al. This also agrees with the relatively high Fe and Ni, but low Cr, concentrations measured for the whole volume (Table 2). Due to the higher initial Cr content relative to Ni, it should be more likely to encounter a region rich in Cr than rich in Ni. It is thus not surprising that Ni-rich regions like the ones observed in this work were not encountered by Sundell et al. [15], and, due to the high Fe content (Table 1) and the propensity of Fe being the first element to dissolve from SPPs, it is not surprising that Fe is the alloying element of highest concentration in both Fe–Ni and Fe–Cr clusters.

Although not mentioned in the paper by Harte et al., it appears from Figure 9 in [4] that clusters of Fe and Ni in proton-irradiated Zircaloy-2 are elongated approximately in the [0001] direction, whereas clusters rich in Cr are smaller and not elongated in any particular direction. This might correspond to our observed two cluster types. The presence of small amounts of Ni in the Fe–Cr clusters and very small amounts of Cr in the Fe–Ni clusters matches the presence of Ni in $Zr(Fe,Cr)_2$ SPPs and the absence of Cr in the $Zr_2(Fe,Ni)$ SPPs observed in [14]. The tendency of forming two different cluster types thus resembles the tendency of forming two different SPP types. For the Fe–Ni clusters, from the observed cluster compositions and the calculated number of MLs occupied by each cluster, it can be concluded that, unlike SPPs, they are not separate phases but can be regarded as a segregation inside the loop. This is in line with the modelling results in [17,18], where Fe and Ni were predicted to accumulate inside loops similar in size to that of our Fe–Ni clusters. The Fe–Cr clusters might, instead, be very small precipitates with a nucleation associated with the loops. Our results also agree with the predicted segregation of Fe (but not Cr or Sn) to prismatic stacking faults by March-Rico et al. but not with their predicted absence of Ni segregation [19].

As a final comment it can be mentioned that the reconstruction was made assuming the hexagonal α-Zr structure, although it is likely that the material at the time of analysis was a hydride. It is well known that hydrogen analysis in APT is difficult, so identification of the correct hydride phase might not be accomplished only by looking at the hydrogen content. As underestimation of the hydrogen content is unlikely but overestimation possible, the specimen seems to have been α-Zr, a ζ-hydride, or a γ-hydride. For the ζ-hydride, which has been observed to have trigonal symmetry and to be fully coherent with the α-Zr matrix [69], the observed crystallographic poles on the hit map would be the same as those of α-Zr, and the interplanar distances and interplanar angles of the identified poles would be similar to those of α-Zr. If the specimen was a γ-hydride, which has face-centred tetragonal (FCT) structure [56], our results would not be considerably changed. This is clear since the <a>-loops are known to align in layers that are normal to the <c>-direction of the Zr metal matrix [2,4], which means that our observed main pole would correspond to the (111) pole in the FCT γ-hydride and that the Fe–Ni discs would still be located in directions approximately 60° apart from each other in the FCT structure. (This would also be the case for the other hydride phases, δ and ε, which have FCC and FCT structures, respectively [56].) Our observations should thus be valid irrespective of which hydride phase they were made in.

6. Conclusions

In this study of a region rich in Ni and Fe in the metal close to the metal/oxide interface in Zircaloy-2 exposed to BWR operation, clusters of Fe and Ni and clusters of Fe and Cr aligned in layers parallel to the basal planes have been observed using APT in voltage mode. A difference in cluster shape between Fe–Ni clusters and Fe–Cr clusters was apparent. The Fe–Ni clusters were disc-shaped, while the Fe–Cr clusters were spheroidal. Typical diameters of the Fe–Ni discs and the Fe–Cr spheroids were 5–15 nm and 5 nm, respectively. Both types of clusters were located at expected positions of <a>-loops, and the Fe–Ni clusters have been shown to be located on planes that are close to all three families of first-order prismatic planes but inclined at angles ranging from 7° to 36° to the [0001] direction. Fe–Cr clusters and all three families of Fe–Ni clusters were located in the same layers. The concentration of Fe in at.% was higher in the Fe–Cr clusters than in the Fe–Ni clusters. Also the total number of Fe, Cr, and Ni atoms/nm^3 was higher in the Fe–Cr clusters. No significant enrichment of Sn in the clusters was found.

Declaration of Competing Interest

None.

CRediT authorship contribution statement

J. Eriksson: Formal analysis, Investigation, Writing - original draft, Writing - review & editing, Visualization. **G. Sundell:** Investigation. **P. Tejland:** Investigation, Resources. **H.-O. Andrén:** Conceptualization, Writing - review & editing, Supervision, Project administration, Funding acquisition. **M. Thuvander:** Conceptualization, Writing - review & editing, Supervision, Project administration, Funding acquisition.

Acknowledgements

This work was performed in part at the Chalmers Materials Analysis Laboratory, CMAL. Material was made available via Westinghouse Electric Sweden AB. Financial support was provided by Westinghouse Electric Sweden AB, Vattenfall AB, OKG AB, and EPRI. The MUZIC consortium is acknowledged for collaboration. Dr Torben Boll is acknowledged for fruitful discussions on APT reconstruction.

References

[1] M. Griffiths, J. Nucl. Mater. 159 (1988) 190–218.
[2] A. Jostsons, P.M. Kelly, R.G. Blake, J. Nucl. Mater. 66 (1977) 236–256.
[3] A. Jostsons, R.G. Blake, J.G. Napier, P.M. Kelly, K. Farrell, J. Nucl. Mater. 68 (1977) 267–276.
[4] A. Harte, D. Jädernäs, M. Topping, P. Frankel, C.P. Race, J. Romero, L. Hallstadius, E.C. Darby, M. Preuss, Acta Mater. 130 (2017) 69–82.
[5] B. Wadman, H.-O. Andrén, ASTM STP 1132 (1991) 461–475. https://www.scopus.com/record/display.uri?eid=2-s2.0-0026386697&origin=resultslist.
[6] R.M. Kruger, R.B. Adamson, S.S. Brenner, J. Nucl. Mater. 189 (1992) 193–200.
[7] B. Hutchinson, B. Lehtinen, M. Limbäck, M. Dahlbäck, ASTM STP 1505 (2009) 269–284.
[8] M. Ivermark, Characterisation of the Matrix Chemistry in Zirconium Alloys Ph.D. Thesis, University of Manchester, 2009.
[9] G. Sundell, Atomic Scale Degradation of Zirconium Alloys for Nuclear Applications Ph.D. Thesis, Chalmers University of Technology, 2015.
[10] C. Lemaignan, A.T. Motta, Zirconium alloys in nuclear applications in materials science and technology – a comprehensive treatment, in: R.W. Cahn, P. Haasen, E.J. Kramer (Eds.), Volume 10B: Nuclear Materials Part II (Chapter 7), B.T. Frost, 1994.
[11] M. Griffiths, R.W. Gilbert, G.J.C. Carpenter, J. Nucl. Mater. 150 (1987) 53–66.
[12] Y. Etoh, S. Shimada, J. Nucl. Mater. 200 (1993) 59–69.
[13] S. Valizadeh, G. Ledergerber, S. Abolhassani, D. Jädernäs, M. Dahlbäck, E.V. Mader, G. Zhou, J. Wright, L. Hallstadius, ASTM STP 1529 (2011) 729–753. https://www.scopus.com/record/display.uri?eid=2-s2.0-84857982773&origin=resultslist.
[14] A. Harte, M. Topping, P. Frankel, D. Jädernäs, J. Romero, L. Hallstadius, E.C. Darby, M. Preuss, J. Nucl. Mater. 487 (2017) 30–42.
[15] G. Sundell, M. Thuvander, P. Tejland, M. Dahlbäck, L. Hallstadius, H.-O. Andrén, J. Nucl. Mater. 454 (2014) 178–185.
[16] T. Sawabe, T. Sonoda, J. Nucl. Sci. Technol. 55 (2018) 1110–1118.
[17] C. Dai, P. Saidi, Z. Yao, M.R. Daymond, Acta Mater. 140 (2017) 56–66.
[18] C. Dai, F. Long, P. Saidi, L.K. Béland, Z. Yao, M.R. Daymond, Phys. Rev. Mater. 3 (2019) 043602.
[19] J.F. March-Rico, G. Huang, B.D. Wirth, J. Nucl. Mater. 540 (2020) 152339.

[20] R.B. Adamson, C.E. Coleman, M. Griffiths, J. Nucl. Mater. 521 (2019) 167–244.
[21] R.A. Holt, R.W. Gilbert, J. Nucl. Mater. 137 (1986) 185–189.
[22] W.E. Berry, D.A. Vaughan, E.L. White, Corrosion 17 (1961) 109t–117t, doi:10.5006/0010-9312-17.3.81.
[23] B. Cheng, R.B. Adamson, ASTM STP 939 (1987) 387–416.
[24] B.V. Cockeram, P.D. Edmondson, K.J. Leonard, B.F. Kammenzind, J.L. Hollenbeck, Nucl. Mater. Energy 19 (2019) 416–432.
[25] B. Wadman, H.-O. Andrén, U. Rolander, Le J. Phys. Colloq. 49 (1988) C6-323–C6-327, doi:10.1051/jphyscol:1988656.
[26] B.V. Cockeram, K.J. Leonard, L.L. Snead, M.K. Miller, J. Nucl. Mater. 433 (2013) 460–478.
[27] I. Mouton, A.J. Breen, S. Wang, Y. Chang, A. Szczepaniak, P. Kontis, L.T. Stephenson, D. Raabe, M. Herbig, T.B. Britton, B. Gault, Microsc. Microanal. 25 (2019) 481–488.
[28] A.J. Breen, I. Mouton, W. Lu, S. Wang, A. Szczepaniak, P. Kontis, L.T. Stephenson, Y. Chang, A.K. da Silva, C.H. Liebscher, D. Raabe, T.B. Britton, M. Herbig, B. Gault, Scr. Mater. 156 (2018) 42–46.
[29] M. Thuvander, H.-O. Andrén, Ultramicroscopy 111 (2011) 711–714.
[30] T. Sawabe, T. Sonoda, S. Kitajima, T. Kameyama, J. Nucl. Mater. 442 (2013) 168–174.
[31] Y. Dong, A.T. Motta, E.A. Marquis, J. Nucl. Mater. 442 (2013) 270–281.
[32] A. Harte, R.P. Babu, C.A. Hirst, T.L. Martin, P.A.J. Bagot, M.P. Moody, P. Frankel, J. Romero, L. Hallstadius, E.C. Darby, M. Preuss, J. Nucl. Mater. 510 (2018) 460–471.
[33] Z. Yu, T. Kim, M. Bachhav, X. Liu, L. He, A. Couet, Corros. Sci. 173 (2020) 108790.
[34] E.J. Kautz, B. Gwalani, S.V.M. Lambeets, L. Kovarik, D.K. Schreiber, D.E. Perea, D. Senor, Y.-S. Liu, A.K. Battu, K.-P. Tseng, S. Thevuthasan, A. Devaraj, NPJ Mater. Degrad. 4 (2020) 29, doi:10.1038/s41529-020-00133-6.
[35] K. Lindgren, K. Stiller, P. Efsing, M. Thuvander, Microsc. Microanal. 23 (2017) 376–384, doi:10.1017/S1431927617000162.
[36] A. Shariq, S. Mutas, K. Wedderhoff, C. Klein, H. Hortenbach, S. Teichert, P. Kücher, S.S.A. Gerstl, Ultramicroscopy 109 (2009) 472–479.
[37] S. Abolhassani, D. Gavillet, F. Groeschel, P. Jourdain, H.U. Zwicky, in: Proc. Int. Top. Meet. LWR Fuel Performance, April 10–13, Park City, Utah, USA, 2000, pp. 470–484. https://scholar.google.com/scholar_lookup?title=Recent%20observation%20on%20the%20evolution%20of%20the%20secondary%20phase%20particles%20in%20Zircaloy-2%20under%20irradiation%20in%20a%20BWR%20up%20to%20a%20high%20burn-up&publication_year=2000&author=S.%20Abolhassani&author=D.%20Gavillet&author=F.%20Groeschel&author=P.%20Jourdain&author=H.U.%20Zwicky.
[38] G. Ledergerber, S. Abolhassani, M. Limbäck, R.J. Lundmark, K.-.Å. Magnusson, J. Nucl. Sci. Technol. 43 (2006) 1006–1014.
[39] G. Kuri, C. Degueldre, J. Bertsch, S. Abolhassani, Appl. Phys. A Mater. Sci. Process. 98 (2010) 625–633.
[40] G. Ledergerber, S. Valizadeh, J. Wright, M. Limbäck, L. Hallstadius, D. Gavillet, S. Abolhassani, F. Nagase, T. Sugiyama, W. Wiesenack, T. Tverberg, in: LWR Fuel Perform. Meet./Top Fuel/WRFPM, Orlando, Florida, USA, 2010, pp. 513–524.
[41] S. Abolhassani, G. Bart, J. Bertsch, M. Grosse, L. Hallstadius, A. Hermann, G. Kuri, G. Ledergerber, C. Lemaignan, M. Martin, S. Portier, C. Proff, R. Restani, S. Valance, S. Valizadeh, H. Wiese, ASTM STP 1543 (2015) 540–573.
[42] A. Harte, T. Seymour, E.M. Francis, P. Frankel, S.P. Thompson, D. Jädernäs, J. Romero, L. Hallstadius, M. Preuss, J. Mater. Res. 30 (2015) 1349–1365.
[43] T. Seymour, P. Frankel, L. Balogh, T. Ungár, S.P. Thompson, D. Jädernäs, J. Romero, L. Hallstadius, M.R. Daymond, G. Ribárik, M. Preuss, Acta Mater. 126 (2017) 102–113.
[44] M. Chollet, S. Valance, S. Abolhassani, G. Stein, D. Grolimund, M. Martin, J. Bertsch, J. Nucl. Mater. 488 (2017) 181–190.
[45] A. Baris, S. Abolhassani, Y.L. Chiu, H.E. Evans, Mater. High Temp. 35 (2018) 14–21, doi:10.1080/09603409.2017.1392412.
[46] A. Garner, F. Baxter, P. Frankel, M. Topping, A. Harte, T. Slater, P. Tejland, J.E. Romero, E.C. Darby, A. Cole-Baker, M. Gass, M. Preuss, ASTM STP 1597 (2018) 491–523.
[47] M. Topping, A. Harte, P. Frankel, C. Race, G. Sundell, M. Thuvander, H.-O. Andrén, D. Jädernäs, P. Tejland, J.E. Romero, E.C. Darby, S. Dumbill, L. Hallstadius, M. Preuss, ASTM STP 1597 (2018) 796–822.
[48] A. Baris, R. Restani, R. Grabherr, Y.L. Chiu, H.E. Evans, K. Ammon, M. Limbäck, S. Abolhassani, J. Nucl. Mater. 504 (2018) 144–160.
[49] G. Kuri, H. Ramanantoanina, J. Bertsch, M. Martin, I. Panas, Corros. Sci. 143 (2018) 200–211.
[50] A. Baris, S. Abolhassani, R. Grabherr, R. Restani, R. Schäublin, Y.L. Chiu, H.E. Evans, K. Ammon, M. Limbäck, Causes of increased corrosion and hydrogen uptake of Zircaloy-2 cladding at high burnups — A comparative study of the chemical composition of a 3 cycle and a 9 cycle claddin, TopFuel, Prague Czech Republic, ENS, 2018. https://www.euronuclear.org/archiv/topfuel2018/fullpapers/TopFuel2018-A0172-fullpaper.pdf.
[51] A.W. Colldeweih, A. Baris, P. Spätig, S. Abolhassani, Mater. Sci. Eng. A 742 (2019) 842–850.
[52] J. Hawes, A. Baris, Y.L. Chiu, S. Abolhassani, J. Nucl. Mater. 534 (2020) 152133.
[53] L. Walters, S.R. Douglas, M. Griffiths, ASTM STP 1597 (2018) 676–690.
[54] K. Thompson, D. Lawrence, D.J. Larson, J.D. Olson, T.F. Kelly, B. Gorman, Ultramicroscopy 107 (2007) 131–139.
[55] D.R. Kingham, Surf. Sci. 116 (1982) 273–301.
[56] J. Bair, M. Asle Zaeem, M. Tonks, J. Nucl. Mater. 466 (2015) 12–20.
[57] H.H. Shen, X.T. Zu, B. Chen, C.Q. Huang, K. Sun, J. Alloys Compd. 659 (2016) 23–30.
[58] S.M. Hanlon, S.Y. Persaud, F. Long, A. Korinek, M.R. Daymond, J. Nucl. Mater. 515 (2019) 122–134.
[59] M. Christensen, W. Wolf, C. Freeman, E. Wimmer, R.B. Adamson, L. Hallstadius, P.E. Cantonwine, E.V. Mader, J. Phys. Condens. Matter 27 (2015) 025402.
[60] J. Zheng, X. Zhou, L. Mao, H. Zhang, J. Liang, L. Sheng, S. Peng, Int. J. Hydrogen Energy 40 (2015) 4597–4604.
[61] P. Tejland, M. Thuvander, H.-O. Andrén, S. Ciurea, T. Andersson, M. Dahlbäck, L. Hallstadius, ASTM STP 1529 (2011) 595–619, doi:10.1520/JAI102956.
[62] O.C. Hellman, J.A. Vandenbroucke, J. Rüsing, D. Isheim, D.N. Seidman, Microsc. Microanal. 6 (2000) 437–444.
[63] P.M. Kelly, R.G. Blake, Philos. Mag. 28 (1973) 415–426.
[64] D.O. Northwood, R.W. Gilbert, L.E. Bahen, P.M. Kelly, R.G. Blake, A. Jostsons, P.K. Madden, D. Faulkner, W. Bell, R.B. Adamson, J. Nucl. Mater. 79 (1979) 379–394.
[65] C. Dai, L. Balogh, Z. Yao, M.R. Daymond, Philos. Mag. 97 (2017) 944–956.
[66] P. Tejland, H.-O. Andrén, J. Nucl. Mater. 430 (2012) 64–71.
[67] P. Tejland, H.-O. Andrén, J. Nucl. Mater. 444 (2014) 30–34.
[68] G.M. Hood, J. Nucl. Mater. 159 (1988) 149–175.
[69] Z. Zhao, M. Blat-Yrieix, J.P. Morniroli, A. Legris, L. Thuinet, Y. Kihn, A. Ambard, L. Legras, ASTM STP 1505 (2009) 29–50.